Int J Fract (2021) 227:39–55
https://doi.org/10.1007/s10704-020-00494-8

ORIGINAL PAPER

An incremental elastic–plastic triaxiality dependent fatigue model

I. S Nijin · Anuradha Banerjee

Received: 20 April 2020 / Accepted: 17 October 2020 / Published online: 8 November 2020

Abstract A stress-state dependent cyclic cohesive model, which accounts for accumulation of plasticity, during both tensile as well as compressive deformations, and incorporates accumulation of irreversible damage due to macroscopic plasticity as well as microstructural mechanisms, is formulated. The model is implemented in mode-I plane strain fatigue crack growth simulations. The model is validated by reproducing the effect of retardation in crack growth rates after different combinations of tensile and compressive overloads. We show accurate description of the elastic–plastic behaviour of the process zone is vital, in particular for negative stress ratios subsequent to a tensile over-load, as considerable plasticity occurs in compression at the crack-tip, significantly reducing retardation effects.

Keywords Cohesive zone model · Fatigue · Triaxiality · Stress-state · Overload

1 Introduction

One of the major challenges in life assessment of structural systems is to incorporate the effects of random, large fluctuations or overloads on their residual service life. In the growth of a fatigue crack subject to a loading history with variable amplitudes due to load interaction effects the damage induced by a single fatigue cycle can be significantly different from that induced during constant amplitude loading of the same maximum and minimum stress intensity factor (Skorupa 1998)). For optimum as well as safe use of critical structural components, there is a vital need for development of predictive models that are based on the mechanics of fatigue damage growth under near-service conditions (Elber 1971; Newman 1984; Voorwald et al. 1991; Beden et al. 2009; Sundar 2012).

Several approaches have been adopted to model fatigue damage initiation and growth at different length scales, starting from molecular dynamics simulations based analysis of nano scale fatigue crack growth as reviewed in (Horstemeyer et al. 2010) to damage mechanics based simulations at macroscopic length scales (Qian et al. 2000; Peerlings et al. 2000; Roe and Siegmund 2003; Pandey et al. 2019). A widely popular phenomenological approach in simulation of fracture and failure processes in a wide range of materials, cohesive zone model (CZM), assumes the damage processes to be localised within a thin layer and the constitutive behaviour of this layer is approximated with an assumed traction–separation law (TSL). As per all different assumed forms of TSL in existing literature, traction increases monotonically with separation till cohesive strength, (σ^{max}), is reached. Further separation between the layer boundaries results in decrease in traction until it vanishes and the boundaries become

I. S Nijin · A. Banerjee (✉)
Indian Institute of Technology Madras, Chennai, India
e-mail: anuban@iitm.ac.in

I. S Nijin
e-mail: nijinis.91@gmail.com

traction-free, implying formation of traction-free fracture surfaces (Park and Paulino 2011). The area under the TSL curve, cohesive energy (Γ_0) and σ^{max} are considered to be the cohesive model parameters that describe the fracture behaviour of the material system completely. The applicability of CZM was extended in prediction of fatigue crack growth curves by accounting for accumulation of irreversible micro-structural damage due to cyclic loading (De-Andrés et al. 1999). By formulating a cohesive law that exhibited unloading-reloading hysteresis, it was possible to prevent shake-down and spurious crack arrest in the simulation during steady-state fatigue crack growth (Nguyen et al. 2001). Further, by introducing an incremental fatigue damage evolution law based on continuum damage mechanics principles (Lemaitre 2012), Roe and Siegmund (2003) developed a cohesive model for fatigue that has been used extensively in prediction of fatigue crack growth behaviour of interfaces like adhesive bonded joints, solder joints, weld joints and materials like composites, polymers and metal alloys etc.

Cyclic cohesive zone model has also been extended to gain an insight into the frequency and time effects by introducing additional incremental damage as a consequence of creep within the cyclic damage parameter (Bouvard et al. 2009). By implementing cyclic CZM in extended finite element method (XFEM), it was shown to be possible for a new crack surface to originate in arbitrary locations and directions without remeshing (Xu and Yuan 2009; Li and Yuan 2013). Extension of cyclic cohesive modelling to 3D allowed simulation of more details like the evolving shape of the crack front (Liu et al. 2009; Yuan and Li 2018). However, in their review of 3D cohesive modelling of fatigue crack growth, Yuan and Li (2018) conclude that the influence of the 3D crack configuration is not as strong in fatigue as in monotonic ductile fracture.

Retardation in the rate of fatigue crack growth due to tensile overloads, simulated using cyclic cohesive zone models, was attributed to growth in the plastic zone size near the crack tip (Nguyen et al. 2001; Ural et al. 2009; Jiang et al. 2009; Li et al. 2017). As a consequence, compressive residual stresses developed during unloading resulted in slowdown in the subsequent crack growth. Li et al. (2017) were able to find cohesive parameters which could validate the experimental crack growth behavior for constant amplitude loading and also for variable amplitude loading with a single overload. However in these studies, the overload was tensile only, thus, compressive overloads and sequential effect of tensile and compressive overload were not considered.

The effect of the constraint of stress-state characterised by $T-$stress, the non-singular term of the crack-tip field, has been investigated experimentally on specimens such as compact-tension (CT), corner notched (CN), central cracked panel (MT) and cruciform specimens of various metal alloys. While the crack growth rates were found to be higher for high constraint conditions in some studies (Tong 2002; Shlyannikov and Zakharov 2014), Miarka et al. (2020) and Hutař et al. (2006) report the rates to be lower. One of the limitations of these studies was that the opening stress at the crack tip and triaxiality were not controlled independently and, thus, the effects reported are due to the coupled action of opening stress as well as the constraint of the stress-state at the crack tip. However, in all the investigations, the fatigue crack exhibited tunnelling effect which is indicative of faster growth of fatigue damage at the central plane where the constraint or triaxiality of the stress-state is highest across the thickness of the specimen.

To incorporate the effect of stress-state on fatigue damage nucleation and growth, a triaxiality dependent cohesive law was utilised in combination with an irreversible damage parameter to account for fatigue damage accumulation (Jha and Banerjee 2012). In the implementation of the model as interface elements, triaxiality parameter of the neighbouring continuum elements (Banerjee and Manivasagam 2009; Siegmund and Brocks 1999; Anvari et al. 2006) as well as shape parameters were utilised (Roth and Kuna 2017). In triaxiality dependent cohesive laws, traction was taken to be not only a function of separation but also a function of the triaxiality parameter such that the conventional cohesive parameters (σ^{max}, Γ_0) were not constants but depend on the stress-state (Banerjee and Manivasagam 2009; Siegmund and Brocks 1999; Anvari et al. 2006). Combining the stress-state dependent cohesive model with an irreversible damage parameter in the formulation, a model for fatigue was developed (Jha and Banerjee 2012). Crack growth curves, based on FEM implementation, for a combination of fatigue damage model parameters, were validated with experimental data of an Aluminium alloy. It was shown that cohesive laws that do not account for effects of stress-state were inadequate as they could either predict the initiation life well or the rate of propagation (Nijin et al. 2019). Further

examining the mechanistic aspects of crack initiation, a meso-scopic length scale was identified that corresponded with the sub-surface location of initiation in the simulations and the location of highest roughness from the notch root in the fracture surface profile data Nijin and Banerjee (2020). Since these investigations were based on positive load ratios, there was limited plasticity experienced during the compressive part of the cycle. Thus, even though the model did not account for plasticity in compression, the results were reliable. If applied in case of overloads, however, where significant plasticity in compression is inevitable, such a model would be inadequate.

Can a cohesive model be formulated that incorporates accumulation of plasticity during compressive deformations as well in its traction–separation behaviour and thereby closely reproduce the elastic–plastic response of the process zone? In modelling the trends of fatigue crack growth after different combinations of tensile and compressive overloads, does the plasticity in compression have a strong influence? In the present study a triaxiality dependent cyclic cohesive zone model, incorporating the hardening behaviour under both tensile as well as compressive loads, is formulated in an incremental form. The deterioration of the cohesive properties is taken to be based on a damage evolution law accounting for both macroscopic damage growth as well as microscopic damage growth over a large number of cycles of subcritical loads. Plane strain finite element simulations of sequential effect of tensile and compressive overloads are performed using cohesive interface element based on elastic-plastic cyclic cohesive zone model (EL-PL CCZM). A discussion is developed on the need of a more accurate description of the elastic–plastic response of the process zone in prediction of overload effects, particularly in case of negative stress ratios.

2 Elastic–plastic Cyclic Cohesive Zone Model (EL-PL CCZM)

In the present work, to be able to simulate the effect of an overload on the growth of a fatigue crack in a ductile solid, we introduce the constitutive framework for an elastic–plastic triaxiality dependent cyclic cohesive zone model which aims to:

- Reproduce elasticity, strain hardening behaviour of the process zone in tension as well as compression by using the Hookean linear elasticity and Mises plasticity constitutive relations in the incremental form
- Account for damage growth due to macroscopic plastic strains as well as accumulation of microstructural damage in absence of macroscopic plasticity as in case of high cycle fatigue
- Account for coupling of damage and elasto-plastic behaviour based on the concept of effective stress and implement it using return map algorithm

2.1 Elastic–plastic behaviour of the cohesive zone

Consider a unit cell of the process zone subject to a stress-state such that principal directions are along the process zone length (x_1), normal to cohesive surfaces (x_2) and in the out of plane thickness direction (x_3) as shown in Fig. 1. As per the present model, opening cohesive traction is taken to depend on the normal separation, the stress-state as described by stress-ratio parameters, $\alpha = \frac{\sigma_{11}}{\sigma_{22}}$, $\beta = \frac{\sigma_{33}}{\sigma_{22}}$, $\hat{\alpha} = \frac{\dot{\sigma}_{11}}{\dot{\sigma}_{22}}$, $\hat{\beta} = \frac{\dot{\sigma}_{33}}{\dot{\sigma}_{22}}$, as well as the current state of damage. The softening behaviour of the traction–separation law and the degradation of the elastic stiffness are accounted by a damage parameter, D. Total damage has contributions from both, macroscopic damage, D_m, due to ductile fracture mechanisms as well as microscopic fatigue damage, D_f, that results in overall deterioration of the process zone response. With in the process zone, the elastic modulus, E, and the initial yield limit in uniaxial tension, σ_{y0}, are taken to degrade with the damage parameter to become the effective elastic modulus, $E(1-D)$, and effective initial yield limit, $\sigma_{y0}(1-D)$, as per the effective stress concept of continuum damage mechanics (Lemaitre 2012). The normal separation (δ_n) of the traction–separation behaviour contains an elastic recoverable separation (δ_n^e) and a plastic irrecoverable part (δ_n^p). The cohesive TSL for the process zone is formulated on the basis of the constitutive relation in the opening direction given by:

$$(\epsilon_{22} - \epsilon_{22}^p)E(1-D) = \sigma_{22} - \nu(\sigma_{11} + \sigma_{33}) \tag{1}$$

The incremental form of Eq. 1 takes the form:

$$\begin{aligned}(\dot{\epsilon}_{22} - \dot{\epsilon}_{22}^p)E(1-D) - \dot{D}(\epsilon_{22} - \epsilon_{22}^p)E = \dot{\sigma_{22}} \\ - \nu(\dot{\sigma_{11}} + \dot{\sigma_{33}}) \\ = \dot{\sigma_{22}}\left(1 - \nu\left(\hat{\alpha} + \hat{\beta}\right)\right)\end{aligned} \tag{2}$$

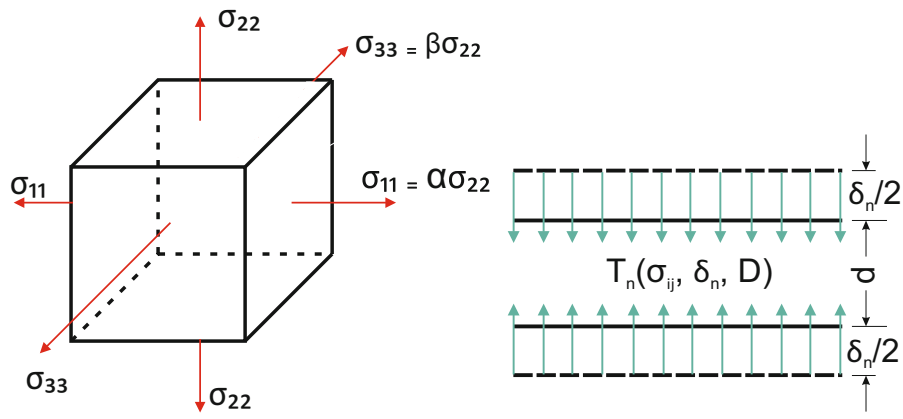

Fig. 1 Schematic representation of the **a** stress-state **b** process zone, where, solid line corresponds to the initial configuration and dashed line corresponds to the deformed configuration

For the process zone, the opening stress, σ_{22}, and the associated direct strain, ϵ_{22}, are the same as the cohesive traction, T_n, and the normalized separation, $\hat{\delta}_n = \delta_n/d$, normalized with void spacing thickness, d, as shown in Fig. 1b, respectively. The incremental form of traction–separation law, thus, can be expressed as:

$$\dot{T}_n = (1-D)\bar{E}(\dot{\hat{\delta}}_n - \dot{\hat{\delta}}_n^p) - \dot{D}\bar{E}(\hat{\delta}_n - \hat{\delta}_n^p), \tag{3}$$

where for simplification $\bar{E} = \frac{E}{1-\nu(\hat{\alpha}+\hat{\beta})}$. Physically, $\bar{E}$ is the effective modulus of resistance to normal separation of the process zone under general state of stress, for uniaxial stress-state $\bar{E}$ simplifies to be the same as E. It is to be noted that in Eq. 3 the traction is expressed as a function of normalised separation, denoted by $\hat{\delta}$, which is dimensionless and $\bar{E}$, thus, has the same dimensions as modulus E. $\hat{\delta}_n^p$ is the inelastic normal separation normalised with void spacing thickness.

2.2 Yield locus and flow rule

To describe the hardening behaviour of the process zone, the yield surface of the ductile solid is assumed to be power-law hardening such that the yield stress, $\sigma_y = \sigma_{y0}\left(1+\frac{\lambda E}{\sigma_{y0}}\right)^n$. Here, σ_{y0} is the initial yield limit, $\lambda = \int \dot{\lambda} dt = \int \sqrt{\frac{2}{3}\dot{\epsilon}_{ij}^p \dot{\epsilon}_{ij}^p}\, dt$, is the equivalent plastic strain, $\dot{\lambda}$ is the plastic multiplier and n is the strain hardening exponent. Yielding of the material is based on the Von Mises criteria, in which material yields when $\sigma_{\text{mises}} > \sigma_y$. For stress-state described in Fig. 1a, σ_{mises} is a scalar computed from the Cauchy stress tensor as $\sqrt{\frac{(\sigma_{11}-\sigma_{22})^2+(\sigma_{33}-\sigma_{22})^2+(\sigma_{11}-\sigma_{33})^2}{2}}$. The damage coupled yield criteria within the process zone is therefore:

$$|\sigma_{22}|\sqrt{\frac{(\alpha-1)^2+(\beta-1)^2+(\alpha-\beta)^2}{2}} > (1-D)\sigma_y \tag{4}$$

Rearranging,

$$|\sigma_{22}| > (1-D)\bar{\sigma}_y, \tag{5}$$

where, $\bar{\sigma}_y = \bar{\sigma}_{y0}\left(1+\frac{\lambda E}{\sigma_{y0}}\right)^n$, with $\bar{\sigma}_{y0} = \frac{\sqrt{2}\sigma_{y0}}{\sqrt{(\alpha-1)^2+(\beta-1)^2+(\alpha-\beta)^2}}$. Physically, $\bar{\sigma}_{y0}$ represents yield limit for σ_{22}, for a general state of stress. The accumulation of plastic strain for the ductile solid is evaluated as per the Levy- Mises flow rule where, the plastic flow in the opening direction is,

$$\begin{aligned}\dot{\epsilon}_{22}^p &= \frac{3}{2}\dot{\lambda}\,\frac{\sigma_{22}-\sigma_{\text{mean}}}{\sigma_{\text{mises}}} \\ &= \frac{3}{2}\dot{\lambda}\,\frac{(2-\alpha-\beta)}{3\sqrt{\frac{(\alpha-1)^2+(\beta-1)^2+(\alpha-\beta)^2}{2}}}\text{sign}(\sigma_{22}),\end{aligned} \tag{6}$$

where, $\sigma_{\text{mean}} = \frac{\sigma_{kk}}{3}$. The yield condition of the traction–separation law is taken to be based on Eq. 5 up to an equivalent plastic strain limit, λ_s, such that the damage coupled yield function is expressed as:

$$\begin{aligned}\Phi :&= |T_n| - (1-D)\bar{\sigma}_y \qquad \lambda < \lambda_s \\ &= |T_n| - (1-D)\bar{\sigma}_y^{max} \qquad \lambda \geq \lambda_s\end{aligned} \tag{7}$$

where, $\bar{\sigma}_y^{max}$ is the maximum traction value of the cohesive law, it corresponds to the value of $\bar{\sigma}_y$ when λ reaches the limit, λ_s. Being the critical plastic strain limit on hardening response of the TSL, λ_s also, therefore, marks the onset of the softening behaviour. It

is to be noted that λ_s is also triaxiality dependent as expressed later in Eq.10. Further, based on Eq. 6, the flow of inelastic separation in the triaxiality dependent cohesive law can be expressed as:

$$\dot{\delta}_n^p = \frac{3}{2}\,\dot{\lambda}\,\frac{(2-\alpha-\beta)}{3\sqrt{\frac{(\alpha-1)^2+(\beta-1)^2+(\alpha-\beta)^2}{2}}}\mathrm{sign}(\mathrm{T_n}). \tag{8}$$

Dependence of λ_s on stress-state is established here using the equivalent plastic strain failure locus for ductile failure. The locus of equivalent plastic strain of failure, $\bar{\epsilon}_f^{pl}$, is known to exponentially decrease with increase in triaxiality parameter (Hancock and Mackenzie 1976; Hancock and Brown 1983), $H = \frac{\sigma_{\mathrm{mean}}}{\sigma_{\mathrm{mises}}} = \frac{(1+\alpha+\beta)}{3\sqrt{\frac{(\alpha-1)^2+(\beta-1)^2+(\alpha-\beta)^2}{2}}}$, as

$$\bar{\epsilon}_f^{pl} = Ce^{-1.5H}, \tag{9}$$

where C is a non-dimensional material parameter that is to be determined from ductile failure experiments (Hancock and Mackenzie 1976). In the triaxiality dependent cohesive model the limit, λ_s, is taken to the same as $\bar{\epsilon}_f^{pl}$, such that

$$\lambda_s = Ce^{-1.5H}. \tag{10}$$

This description of onset of softening behaviour in a triaxiality dependent cohesive model has been shown to well reproduce experimental data on both plane strain notched bars as well as fracture test specimens (Rashid and Banerjee 2013, 2017). The critical plastic strain is calibrated in a previous study on monotonic ductile fracture using the ductile fracture experimental data of notched bars and compact tension specimens (Rashid and Banerjee 2017). For the current study we use the same calibrated critical plastic strain as well as elastic–plastic behaviour for the representative ductile material.

It has been shown that for an equivalent plastic strain failure locus to be applicable for a wider range of triaxiality parameter, it must also include the effect of Lode parameter (Bao and Wierzbicki 2014; Barsoum and Faleskog 2007). A more recent micro-structural analysis of porous elasto-plastic materials using second-ordered homogenization model shows a significant effect of Lode parameter on critical equivalent plastic strain for failure only at lower triaxality at higher triaxiality the effect is marginal (Danas and Ponte Castañeda 2012). In the present study, since the crack growth simulations were performed for a thick CT specimen, the stress-state was expected to have high triaxiality across most of the thickness, and the effect of Lode parameter was, therefore, ignored.

2.3 Total damage evolution in the process zone

In the early stages of fatigue life of a component subject to sub-critical cyclic loads, damage growth is slow and largely at the microscopic scale. However, at later stages, close to final failure, damage growth involves significant plastic deformation and associated failure mechanisms and finally the local separation occurs when damage reaches a limit at which local instability occurs in the surface leading to sudden local separation. In the present work, we account for both types of damage growth by taking the total damage, D, to constitute of macroscopic damage (D_m) resulting from ductile fracture mechanisms as well as microscopic fatigue damage (D_f) due to sub-critical cyclic loads in absence of any macroscopic plasticity, such that an increment in the damage parameter is $\dot{D} = \dot{D_m} + \dot{D_f}$.

The cohesive element is considered to be completely separated, when, the total damage accumulated reaches a critical damage limit, D_c, which is taken to be 0.25 for the present study, following the estimates for aluminium alloys (Lemaitre 2012). Critical damage limit represents the value of damage at which local instability occurs in the solid leading to sudden local separation.

2.3.1 Damage resulting from macroscopic plasticity (D_m)

Softening behaviour of the process zone is a manifestation of initiation and growth of damage. In the present study, rate of growth of damage in the process zone due to macroscopic plasticity (D_m) is taken to be proportional to the accumulated plastic strain rate beyond the threshold parameter λ_s that is dependent on the stress-state, and up to the critical limit on total damage, D_c (Lemaitre 2012). In the model, monotonic damage is assumed to accumulate only for positive increments of opening separation. However, the equivalent plastic strain accumulates in both tension as well as compression of the process zone. Hence the compression of the process zone can have a significant effect on the onset of the softening behavior for significant plasticity in compression, such as during overloads, as softening starts when $\lambda = \lambda_s$. The overall form of damage evolution is based on the exponential softening behaviour

of the cohesive law formulated for ductile fracture by Banerjee and Manivasagam (2009):

$$\dot{D}_m = \frac{0.02\ \dot{\lambda}}{\epsilon_{y0}+\lambda_s}\left(\frac{\lambda-\lambda_s}{\epsilon_{y0}+\lambda_s}\right)^3 e^{-0.005\left(\frac{\lambda-\lambda_s}{\epsilon_{y0}+\lambda_s}\right)^4} \quad H(\lambda-\lambda_s) \qquad \dot{\delta}_n > 0 \quad = 0 \qquad \dot{\delta}_n \leq 0, \tag{11}$$

where $\epsilon_{y0} = \frac{\sigma_{y0}}{E}$, is the strain limit for linear elastic behaviour. As $\dot{\lambda}$ is always ≥ 0, the irreversibility of damage parameter is ensured. The effect of damage on the traction–separation behaviour is implemented in Eqs. 3 and 7 which ensure that damage degrades the stress-state dependent properties ($\bar{E}$, $\bar{\sigma}_y$ and $\bar{\sigma}_y^{max}$) of the TSL.

As λ_s decays exponentially with triaxiality parameter, at higher triaxiality, D_m initiates at a comparatively lower equivalent plastic strain and also accumulates at a faster rate as per Eqs. 9 and 11 . Representation of the softening behaviour as a component of total damage allows explicit coupling between damage due to multiple failure mechanisms.

The final stages of fatigue crack growth have significant plastic deformation and damage growth ahead of crack tip is due to mechanisms similar to monotonic fracture such as void growth and coalescence. To illustrate the manner of accumulation of damage (D_m) due to macroscopic plasticity (λ) and its effect on the traction–separation behaviour of a typical cohesive element ahead of crack tip, fracture simulation under monotonic mode-I load was performed using the same model parameters as used in the remaining study. As seen in Fig. 2, the traction separation law follows elastic behaviour with stress-state dependent stiffness $\bar{E}/d$, till the stress-state dependent yield limit, $\bar{\sigma}_{y0}$. Subsequent separation causes the equivalent plastic strain (λ) to accumulate resulting in hardening behaviour, where traction follows non-linear hardening response as per $\bar{\sigma}_y$. The change of slope in the traction–separation curve, observed during hardening is due to onset of plasticity induced in the neighbouring continuum elements. Similar change in slope has been observed in earlier studies using stress-state dependent cohesive models (Siegmund and Brocks 2000). The onset of damage accumulation starts when the accumulated equivalent plastic strain reaches the critical limit, λ_s. When accumulated plastic strain reaches λ_s, the traction reaches its maximum limit $\bar{\sigma}_y^{max}$. Subsequent separation results in the accumulation of damage thereby degrading the traction bearing capacity of the cohesive elements as $(1-D)\bar{\sigma}_y^{max}$, as shown in the Fig. 2.

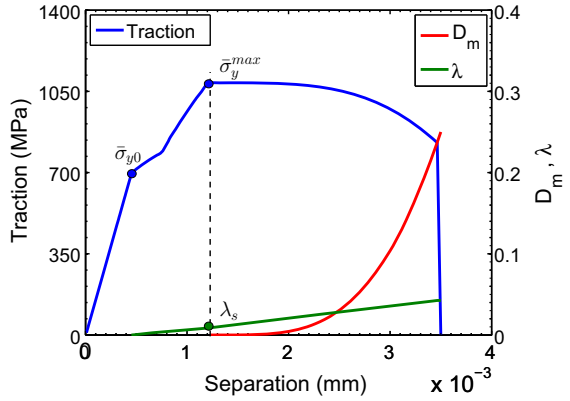

Fig. 2 Variations in traction, λ and D_m with separation at crack tip for monotonic fracture simulations using model parameters used in the present study that reproduces monotonic fracture data in (Rashid and Banerjee 2017)

2.3.2 *Microscopic fatigue Damage (D_f)*

Accumulation of microscopic damage due to cyclic deformations occurs even in absence of macroscopic plasticity as in case of high cycle fatigue. Here the growth of microscopic fatigue damage is based on the damage law, with stress-state dependent cohesive parameters, formulated and implemented in earlier studies (Nijin et al. 2019; Nijin and Banerjee 2020). Incremental damage is taken to be related to the incremental total separation ($\dot{\delta}_n$) normalised with a fatigue cohesive length model parameter, δ_Σ, as

$$\dot{D_f} = \frac{\langle\dot{\delta}_n\rangle}{\delta_\Sigma}\ H\left(\delta_{acc}-\Delta_0\right) \qquad T_n \geq \sigma_f \quad = 0 \qquad T_n < \sigma_f \tag{12}$$

Only positive incremental separation above the fatigue cohesive model parameter referred as the cohesive fatigue endurance limit, σ_f, is considered to contribute in the accumulation of damage and the condition is implemented using Macaulay brackets ($\langle\ \rangle$). Also, fatigue damage is assumed to accumulate only when the accumulated separation, $\delta_{acc} = \int \langle\dot{\delta}_n\rangle\ H\left(T_n\right) dt$, reaches a fatigue threshold parameter Δ_o and the condition is achieved using the Heaviside function, $H(x)$.

The form of Eq. 12 has similarities to (Roe and Siegmund 2003; Siegmund 2004; Li et al. 2017; Jiang et al.

2009; Xu and Yuan 2009; Li and Yuan 2013), however, the fatigue cohesive model parameters here, δ_Σ, Δ_0 and σ_f, are not material constants as they depend on λ_s, and thus, are stress-state dependent. In the present study, the fatigue cohesive model parameters were chosen to be, $\delta_\Sigma = 750\ (\epsilon_{y0} + \lambda_s)d$, $\Delta_0 = 500\ (\epsilon_{y0} + \lambda_s)d$ and $\sigma_f = 0.35\ \bar{\sigma}_y^{max}$, such that initiation life, propagation life and crack growth rates correspond to experimental data for constant amplitude HCF in an Aluminium alloy (Nijin et al. 2019). It is to be noted that as the fatigue cohesive length parameter δ_Σ is orders of magnitude higher than the monotonic separation at λ_s, accumulation of microscopic damage due to subcritical load is very slow and occurs over a large number of cycles. It also implies that large separation induced in a few cycles with macroscopic plasticity while contributes in evolution of macroscopic damage, it can not significantly contribute to the incrementation in microscopic damage.

2.4 Return mapping algorithm for implementation of coupled damage and elasto-plastic behaviour

The aim of the constitutive integration scheme was to solve for the opening traction (T_n) and the internal variables such as equivalent plastic strain (λ) and damage (D) at time $t + \Delta t$, given the variables at time, t, for an opening separation increment of $\dot{\delta}_n$. A fully implicit backward Euler scheme was used to integrate the constitutive equations as the approach is known to be numerically stable even for large increments for a non-linear constitutive relation.

An elastic trial state was assumed, where the increment was taken to be purely elastic and the evolution of the internal variables in the trial state was assumed to be absent. The trial state of the traction increment and the yield function (Φ) take the form:

$$\begin{aligned} \dot{T}_n^{trial} &= (1 - D(t))\ \bar{E}\ \dot{\delta}_n \\ \Phi^{trial} &:= T_n(t) + \dot{T}_n^{trial} \\ &\quad - (1 - D(t))\ \bar{\sigma}_y(\lambda(t)) \qquad \lambda < \lambda_s \\ &:= T_n(t) + \dot{T}_n^{trial} - (1 - D(t))\ \bar{\sigma}_y^{max}(\lambda_s) \qquad \lambda \geq \lambda_s. \end{aligned} \tag{13}$$

The next step of the algorithm was to compare the trial state yield function with the yield condition. If $\Phi^{trial} \leq 0$, then the traction of the cohesive element was within the yield locus and hence the traction and the internal variables were the same as of the trial state. However, if $\Phi^{trial} > 0$, then traction of the cohesive element was outside the yield locus and return mapping algorithm was used to find the internal variables and incremental traction to bring back the traction to the yield locus. For the plastic multiplier, $\dot{\lambda}$ which was required to bring back the traction to the yield locus, the state of traction and internal variables at time, $t + \Delta t$ were taken to be

$$\begin{aligned} T_n(t + \Delta t) &= T_n^{trial}(t+\Delta t) - (1 - D(t+\Delta t))\ \bar{E}\ \dot{\hat{\delta}}_n^p \\ &\quad - \dot{D}_m\ \bar{E}\ (\hat{\delta}_n(t + \Delta t) - \hat{\delta}_n^p(t + \Delta t)) \\ D(t + \Delta t) &= D(t) + \dot{D}_m \\ \hat{\delta}_n^p(t + \Delta t) &= \hat{\delta}_n^p(t) + \dot{\hat{\delta}}_n^p \\ \bar{\sigma}_y(t + \Delta t) &= \bar{\sigma}_{y0}\left(1 + \frac{(\lambda(t) + \dot{\lambda})E}{\sigma_{y0}}\right)^n \end{aligned} \tag{14}$$

where $\dot{\hat{\delta}}_n^p$ and $\dot{D}_m$ are functions of $\dot{\lambda}$ as expressed earlier in Eqs. 8 and 11. As evolution of D_f is slow, the effect of $\dot{D}_f$ in the incremental solution of the traction and internal variables at time, $t + \Delta t$ was ignored within a cycle. The incremental fatigue damage, $\dot{D}_f$, was accumulated over a cycle and the fatigue damage after a complete cycle was updated to be $D_f^{cycle} = D_f^{cycle} + \dot{D}_f$. To reduce the computational effort D_f^{cycle} was scaled for a chosen scaling interval ΔN with the assumption that D_f^{cycle} was not significantly different for the subsequent cycles in the scaling interval, ΔN. Ignoring the higher order terms in Taylor series expansion, the total damage after $N + \Delta N$ was, therefore, updated as: $D_f^{N+\Delta N} = D_f^N + D_f^{cycle}\Delta N$.

The internal variables and traction at the end of time, $t + \Delta t$, were found by solving for $\dot{\lambda}$ iteratively from the non-linear equation of damage coupled yield condition,

$$\begin{aligned} \Phi(t + \Delta t) &:= |T_n(t + \Delta t)| - (1 - D(t + \Delta t)) \\ &\quad \bar{\sigma}_y(t + \Delta t) = 0 \qquad \lambda < \lambda_s \\ &:= |T_n(t + \Delta t)| - (1 - D(t + \Delta t)) \\ &\quad \bar{\sigma}_y^{max}(\lambda_s) = 0 \qquad \lambda \geq \lambda_s, \end{aligned} \tag{15}$$

using Newton-Raphson method. In the implementation of the incremental cohesive law proposed in the present work as interface elements, a complete summary of the traction–separation behaviour is presented as shown in Table. 1 in Appendix A and based on Eqs. 3, 8, 11, 15, the details of the formulation of the consistent tangent operator is presented in Appendix B.

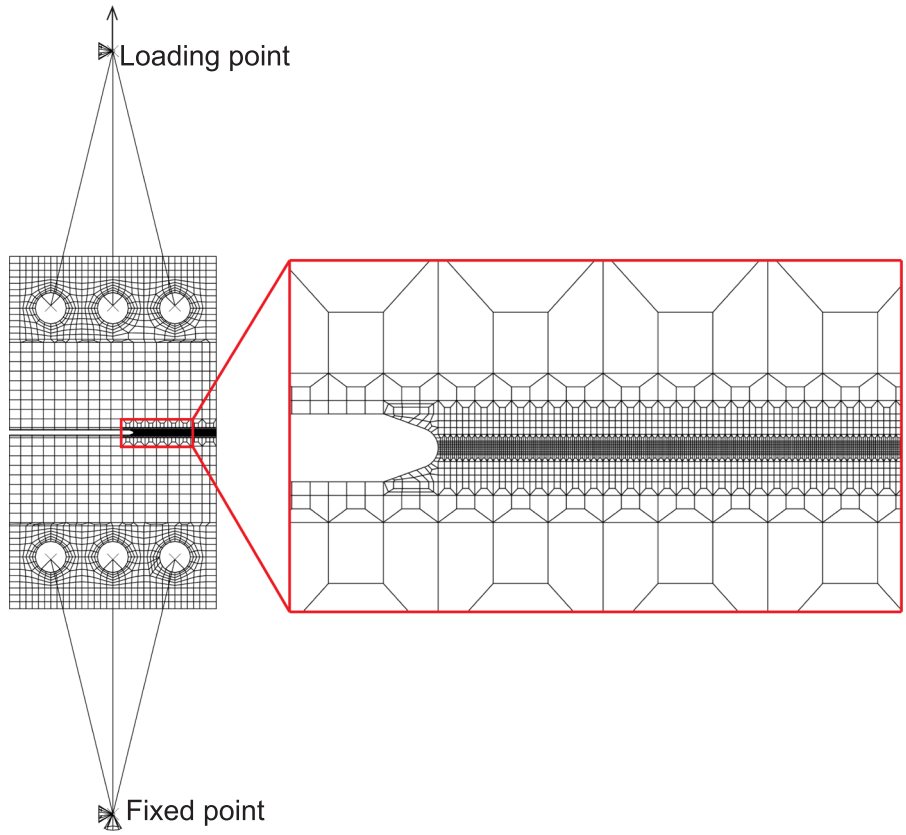

Fig. 3 FEM model of CTS specimen

3 Finite element model

For simulations, a geometry of CTS specimen with V -notch of width = 1 mm, tip radius = 0.3 mm and specimen width, W = 44 mm was modelled in finite element using commercially available software Abaqus 6.11-1 as shown in Fig. 3. Finite element mesh with 9721 quadrilateral plane strain elements was generated in which near the expected crack growth path, the mesh was uniformly refined. Zero thickness cohesive elements of cohesive length 0.03 mm were inserted along the expected crack growth for a mode-I fatigue loading. Elastic–plastic material behaviour (E = 70,000 MPa, $\sigma_y = 281$ MPa, $\nu = 0.33$, $n = 0.164$) for the analysis was taken to be that of a representative aluminium alloy (AA 2219- T87) (Rashid and Banerjee 2017). In the present work isotropic hardening was assumed, however, for more realistic representation of the process zone behaviour the effect of kinematic hardening needs to be incorporated and the related material constants need to be determined from cyclic plasticity data. Quarter pins modelled as rigid surfaces were used to connect the loading point and a fixed point to the specimen geometry using multipoint constraint (MPC) where the quarter pins were also tied to the specimen surface in contact with the pins. The degradation of material properties was accounted in cohesive elements as per EL-PL CCZM with cohesive model parameter, C=0.432 (Rashid and Banerjee 2017) and fatigue damage model parameters ($\sigma_f = 0.35\bar{\sigma}_y^{max}$, $\delta_\Sigma = 750(\epsilon_{y0} + \lambda_s)d$ and $\Delta_o = 500(\epsilon_{y0} + \lambda_s)d$) consistent with (Nijin et al. 2019). The traction–separation of the EL-PL CCZM was incorporated into Abaqus v 6.11-1 using a user element subroutine (UEL) and the contributions of the cohesive elements in global force vector and global stiffness matrix were accounted for in the statement of equilibrium as per virtual work (Needleman 1992). Stress-state of a cohesive element was evaluated from the neighbouring continuum element using another subroutine (UVARM) as implemented earlier in stress-state dependent cohesive models (Nijin et al. 2019; Siegmund and Brocks 1999; Anvari et al. 2006; Rashid and Banerjee 2017, 2013).

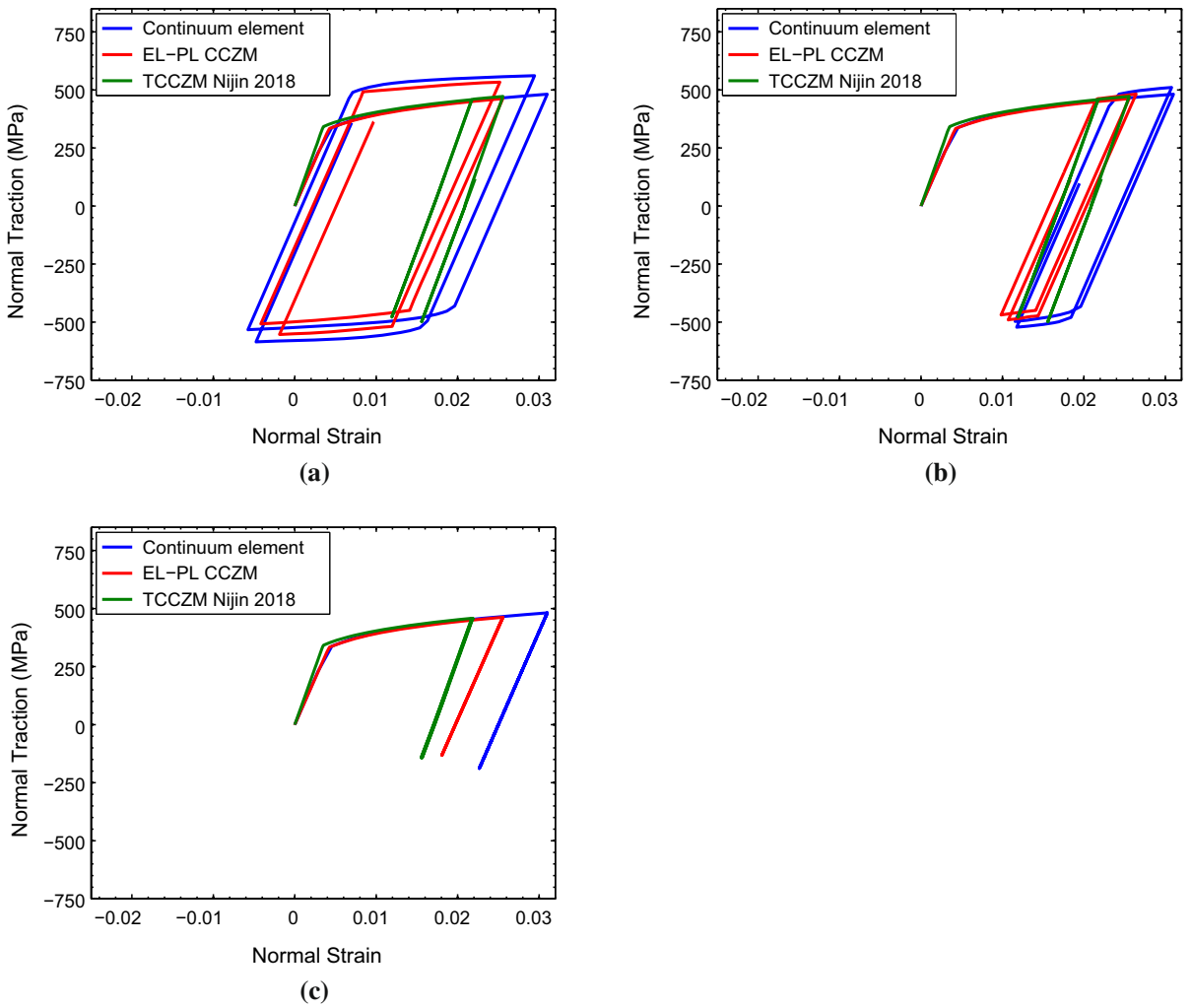

Fig. 4 Evolution of traction and normal strain at the notch tip for load ratios **a** R = −0.5, **b** R =0 and **c** R = 0.5

4 Results and discussion

4.1 Elastic–plastic behaviour of the process zone

To demonstrate the effectiveness of the proposed cohesive model for fatigue in prediction of the elastic–plastic behaviour of the process zone, plane strain simulations were performed for a CTS specimen subject to cyclic loading having load ratios R = -0.5, 0 and 0.5, with the maximum load at 16 kN. The resulting traction-normalised separation response of the model for 2 representative cycles is shown at the notch tip in Fig. 4. The response is also compared with that obtained using TCCZM as in Nijin et al. (2019) as well as with the elastic–plastic analysis without damage modelling.

For the load ratios R= -0.5, 0 the continuum element exhibits plasticity in both tension as well as compression as evident Fig.4a, b. For the same load ratios, the proposed implementation is able to capture both the plasticity in compression. The previous implementation of triaxiality dependent cohesive model for fatigue by Nijin et al. (2019) while is adequate in reproducing the characteristic features for R=0.5, in which the element at the notch tip remains largely in tension and a very small portion of the load cycle develops compressive traction that crosses the plastic limit as shown in Fig. 4c, it is unable to account for the hysteresis loop and the changes in its shape with continued cyclic loading in Fig. 4a, b. The main reasons behind model by Nijin et al. (2019) behaving significantly different

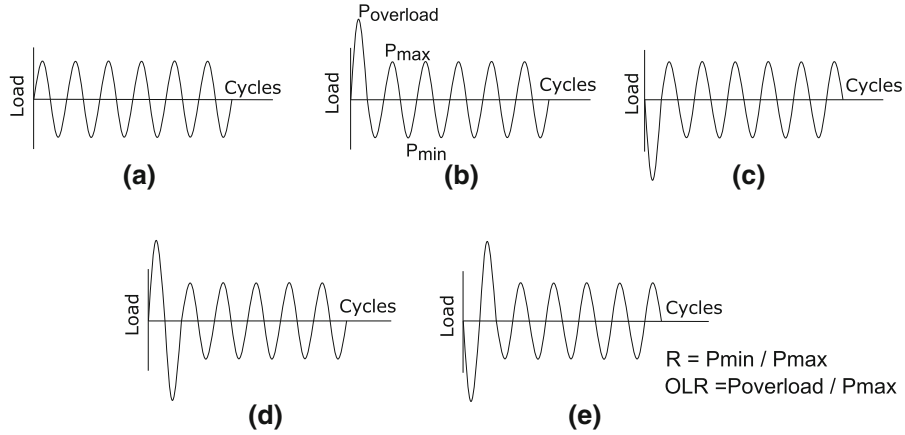

Fig. 5 Loading sequence of R = −1 with **a** no-overload, **b** tensile overload, **c** compressive overload, **d** tension–compression overload and **e** compression–tension overload

from the continuum behaviour at lower load ratios, R = −0.5 and 0, is because it uses only the biaxiality ratio $\alpha(=\frac{\sigma_{11}}{\sigma_{22}})$ to account for the stress-state dependency of the cohesive elements and traction–separation law. Also, the formulation used the approximation of $\nu = 0.5$, to express explicit relation between traction and total separation. Similar approximations were also used in triaxiality dependent cohesive zone models earlier (Siegmund and Brocks 1999; Anvari et al. 2006). The model developed in the present study utilises the stress-state from the nearby continuum elements by using variables $\alpha = \frac{\sigma_{11}}{\sigma_{22}}$, $\beta = \frac{\sigma_{33}}{\sigma_{22}}$, $\hat{\alpha} = \frac{\dot{\sigma}_{11}}{\dot{\sigma}_{22}}$, $\hat{\beta} = \frac{\dot{\sigma}_{33}}{\dot{\sigma}_{22}}$ and is, thus, able to closely reproduce the elastic–plastic behaviour of the nearby continuum element as shown in the Fig. 4. Capability to account for hardening behaviour during compression also, in the proposed traction–separation law, is a significant improvement in cohesive zone modelling as it enables the model to capture the residual stress effects more accurately.

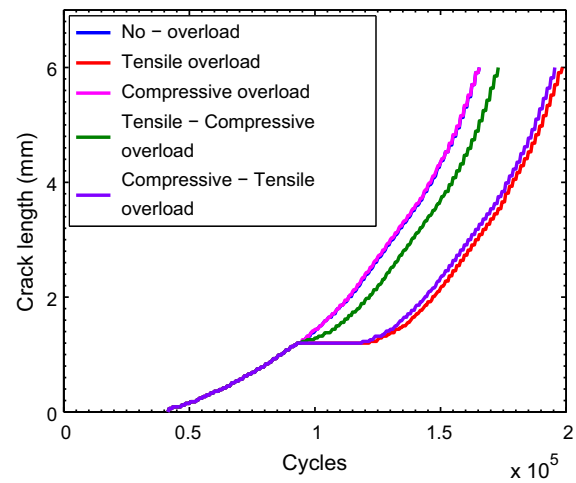

Fig. 6 Simulated crack growth behaviour of precracked specimen of initial crack length 1.2 mm subjected to load sequence with different types of overloads

4.2 Effects of combinations of tensile and compressive overloads on crack growth curves

The model is next used to simulate the well known effects of an overload on the crack growth curves. The CTS specimen was first subjected to 93,000 cycles of sinusoidal load with P_{max} =5 kN and R = 0 such that a fatigue crack of length, $\Delta a = 1.2$ mm was formed. Apart from the no-overload case shown in Fig. 5 (a), four different types of single overloads were simulated: tensile overload, compressive overload, tensile-compressive overload and compressive-tensile overload with overload ratio (OLR) 2 and −2 as shown in Fig. 5b–e.

The simulated crack growth curve predictions are present in Fig. 6. It is evident that, compressive over load does not result in any retardation in the crack growth rate. The tensile overload, in contrast, results in the most pronounced retardation. Retardation in growth rate when a compressive overload follows the tensile overload is higher than when the sequence is compression followed by tension overload. These trends observed in the crack growth simulations using the elastic–plastic triaxiality dependent cyclic cohesive zone model qualitatively agree well with those observed in experimental crack growth data obtained from load interaction effects reported for 2024-T3 and 7075-T6 Aluminium alloys (Stephens et al. 1976).

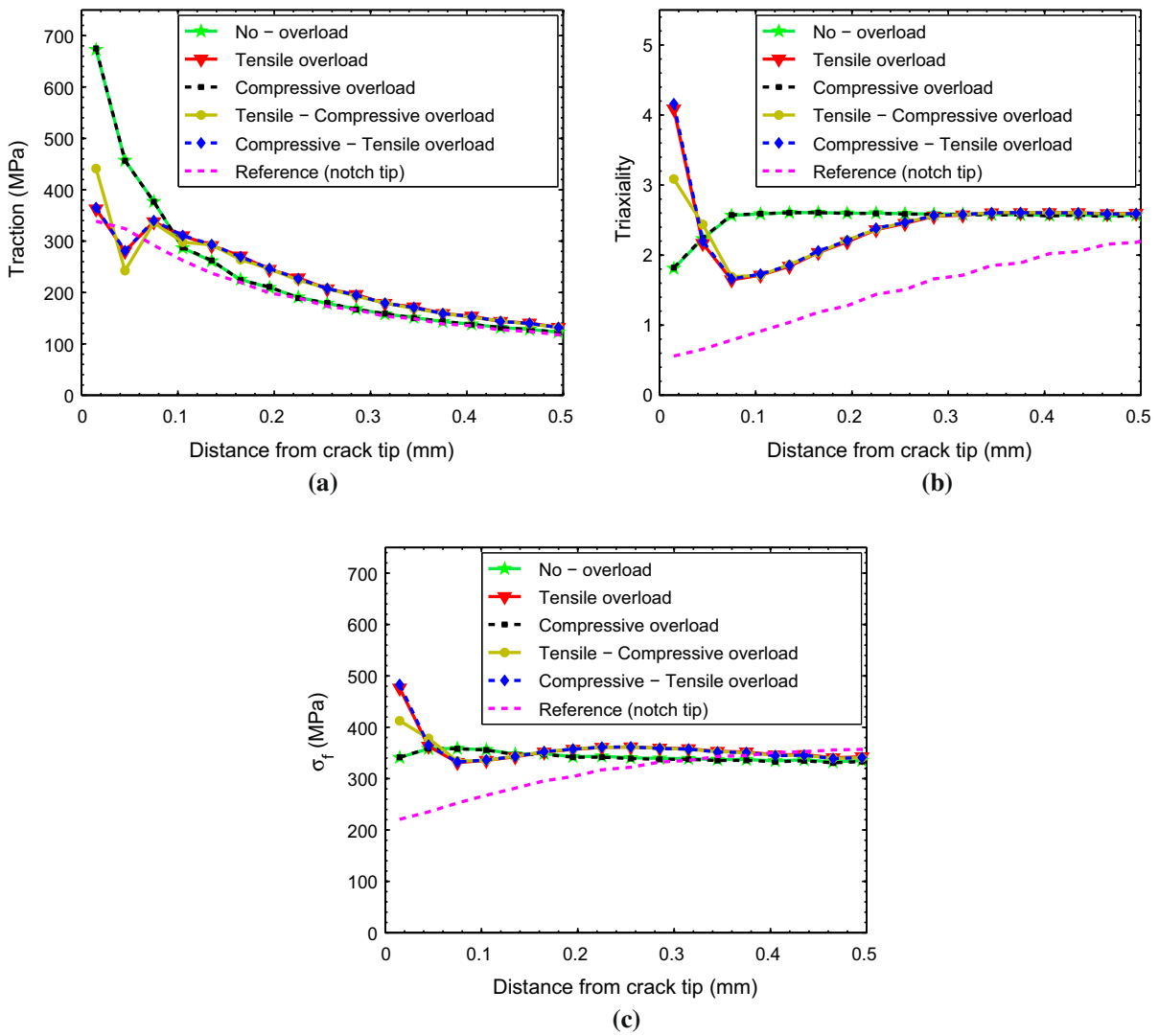

Fig. 7 Variation in **a** the traction, **b** the triaxiality and **c** fatigue cohesive model parameter, σ_f, with the distance from the crack tip for different applied overload combinations

The differences in the retardation rates observed in the simulations are better understood by examining the variation in the opening traction and triaxiality parameter of the stress-state ahead of the crack tip at P_{max} in the cycle subsequent to the different overload cases shown in Fig. 7a, b. Redistribution of traction and triaxiality is observed after the overloads due to the effect of plasticity ahead of the crack. After the tensile overload, the traction of cohesive elements near to the crack tip is significantly reduced while the triaxiality of the cohesive elements at the crack tip is high, ahead of the crack tip. There is, thus, a coupled effect of lower traction as well as higher triaxiality ahead of crack tip for a tensile overload. The specific effect of triaxiality on the overall crack growth curves has been computationally shown in a previous paper (Nijin et al. 2019). This difference results in slower accumulation of microscopic fatigue damage, after a tensile-overload when compared to constant amplitude loading as damage evolves, as described in Eq. 12, only when the current traction level is greater than the fatigue limit parameter. Whereas after a compressive-overload, there is no noticeable change in neither the variation in the open-

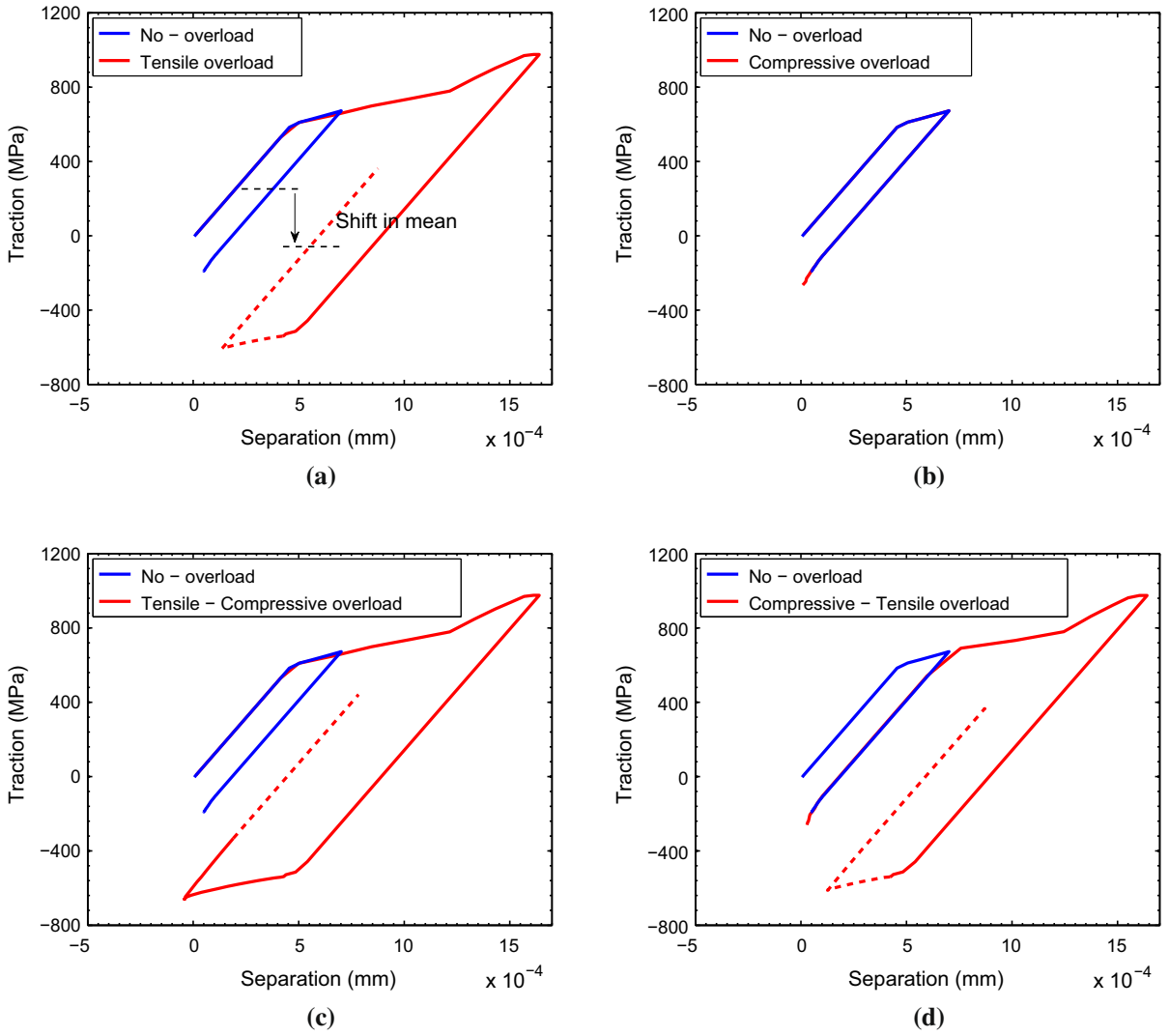

Fig. 8 Traction–separation behaviour of cohesive element ahead of notch tip subjected to load sequence with **a** tensile overload, **b** compressive overload, **c** tension–compression overload and **d** compression–tension overload compared to no-overload condition

ing traction nor the triaxiality ahead of the crack tip when compared with the no overload case.

The significant role of triaxiality has been brought out by including the data for region ahead of notch tip also as a reference in Fig. 7. In Fig. 7b, it is evident that the triaxiality ahead of notch tip, prior to fatigue crack initiation, is significantly lower than for that ahead of crack tip for all the overload cases. The cohesive fatigue endurance limit parameter (see Sect. 2.3.2), σ_f, ahead of crack tip for all overload cases as well as ahead of notch tip prior to initiation of fatigue crack is shown in Fig. 7c. Since the parameter is stress-state dependent and is lower for region ahead of notch tip when compared to ahead of a crack tip for all overload cases, the accumulation of fatigue damage is possible in spite of lower traction ahead of the notch tip.

The traction–separation behaviour of the cohesive element at the crack tip, in the cycle prior to overload (blue coloured curve), during overload (solid red curve) and post overload (dashed red curve), is presented in Fig. 8. In Fig. 8a, compared to the no-overload, the tensile overload has significant non-linear separation up to the peak load of the cycle, subsequent unloading results in development of compressive stresses due

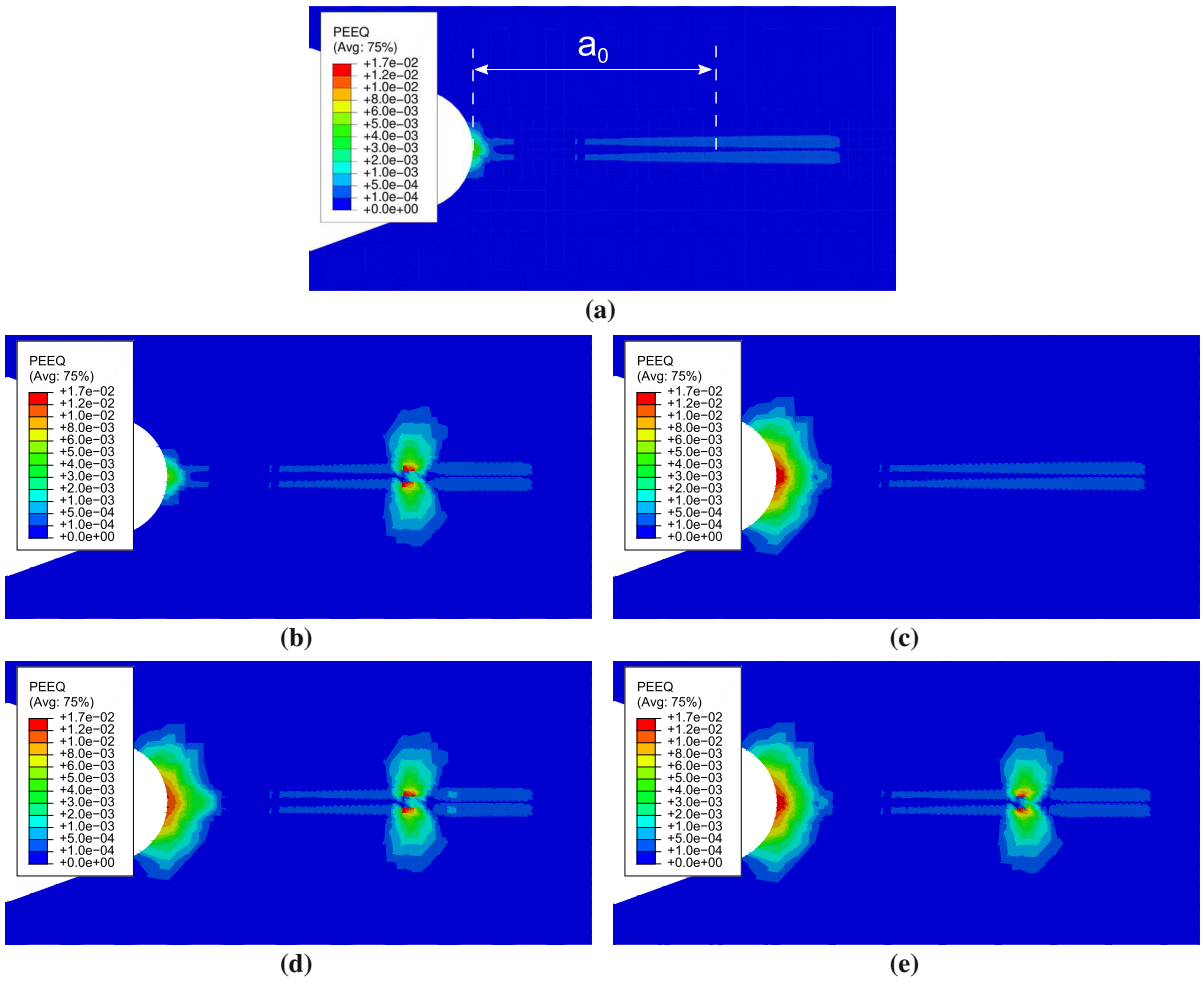

Fig. 9 Spread of opening plastic strain ϵ_{22}^{p} for conditions of **a** no-overload, **b** tensile overload, **c** compressive overload, **d** tension–compression overload and **e** compression–tension overload when propagating crack reaches 1.8 mm

to residual plastic deformation. The change of slope in the traction–separation curve, observed during tensile overload is due to onset of plasticity induced in the neighbouring continuum elements. Similar change in slope has been observed in earlier studies using stress-state dependent cohesive models (Siegmund and Brocks 2000). Post-overload, the resumption of regular loading cycles induces a traction cycle that has significantly lower mean traction compared to no-overload case. The shift in the mean traction is lesser for compressive-tensile overload (Fig. 8d), followed by tensile-compression cycle (Fig. 8c) and the least effect on the traction–separation response ahead of crack tip, as reported in Fig. 8b, is due to the compressive overload which corresponds with no-retardation in the crack growth rates described earlier.

The corresponding equivalent plastic strain contours are presented in Fig. 9. For a precrack, a_o, in absence of any overload, the plastic wake has a uniform band-like appearance on either side of the crack path as seen in Fig. 9a. On account of tensile overload, extensive plastic deformation occurs at $a = a_o$, however in contrast, for compressive overload the plasticity occurs only near the notch root and there is no evidence of overload effect on the crack tip plasticity. During compression, the presence of geometric singularity due to the precrack is not felt as the crack flanks come in contact and the contacting surface are able to transmit negative normal traction due to compression. Tension–compression

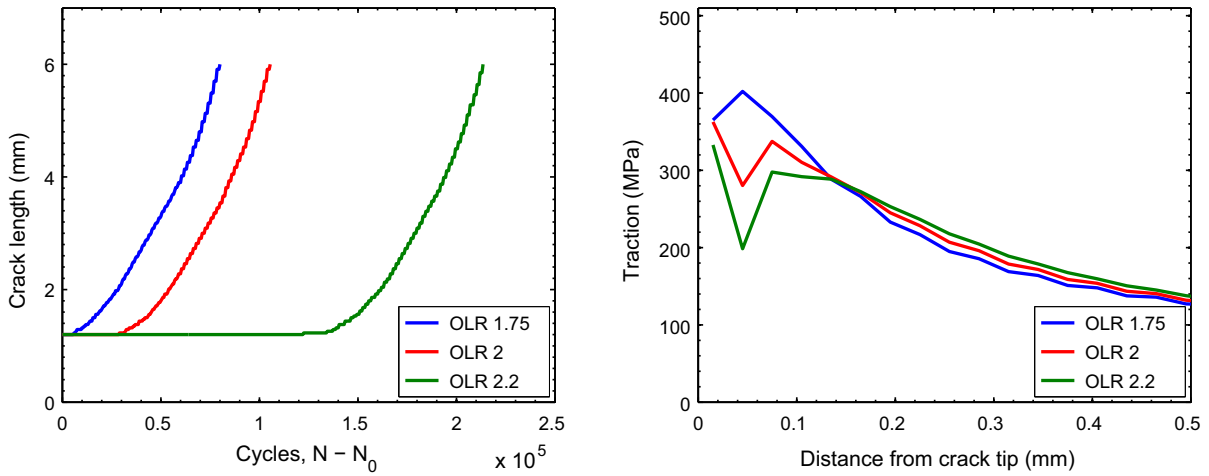

Fig. 10 **a** Simulated crack growth curves of precracked specimen of initial crack length 1.2 mm subjected to load sequence with overload ratio 1.75, 2, 2.2 **b** variation of traction with the distance from the crack tip for same cyclic loading conditions

and compression–tension overloads differ marginally with notch-root plasticity being higher in the latter case as seen in Fig. 9d, e.

4.3 Effects of increasing overload ratio on crack growth curves

Further, the proposed model is applied in prediction of effects of increasing overload ratio by simulating crack growth for overload ratios 1.75, 2, 2.2 with subsequent loading cycles at R = −1. The obtained crack growth curves are presented in Fig. 10a. The retardation in the rate of crack growth is more pronounced for higher OLR which is consistent with the trends reported in experimental literature (Stephens et al. 1976). For each case, post-overload the stresses redistribute differently ahead of crack-tip as shown in Fig. 10b. The opening traction near the crack-tip, at maximum of the load cycle after the overload cycle, decreases with the increase in the overload ratio which results in the increased retardation effect after the tensile overload. The differences in the traction ahead of the crack tip are highest a little ahead of the crack tip.

4.4 Effects of negative load ratio on crack growth curves

Experimentally obtained crack growth data is also known to show diminished retardation effects if after the tensile overload the subsequent cycling has a negative load ratio (Stephens et al. 1976). Simulations for a single tensile overload of OLR = 2.2 followed by different negative load ratios: R = −2, −1, 0 well reproduce the reported reduction in retardation effect as shown in Fig. 11a. By examining the traction–separation response during a cycle prior to overload, the overload and a cycle post-overload as shown in Fig. 11b for each case of subsequent load ratios, the reduction in the retardation effect appears to be primarily due to the plasticity induced at the crack tip in the compression cycle after tensile load. Higher the negative stress-ratio, higher is the plastic separation induced. As a result, in the subsequent cycling in which the behaviour is linear elastic, for R = −2 the cycle has the highest peak tensile stress even though the maximum applied remote load is the same in each case. For R=0, the crack arrests as the cycles subsequent to tensile overload do not develop enough traction for continued damage growth.

5 Concluding remarks

In the present work, we formulate and implement a stress-state dependent cohesive model for fatigue that accounts for plasticity of the process zone in a representative ductile solid under both tension as well as compression. In the model, the constitutive behaviour of the cohesive zone is based on incremental plasticity relations coupled with an evolving irreversible damage

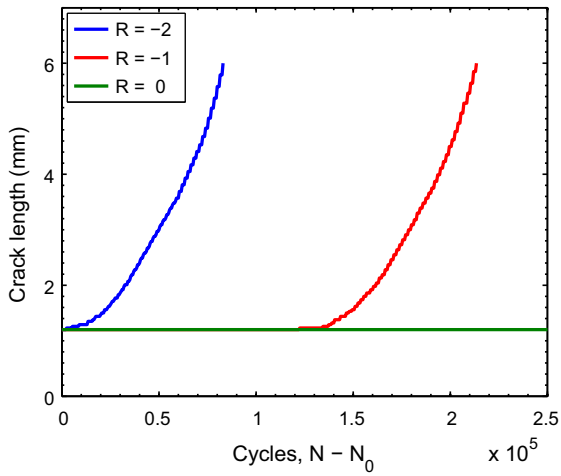

Fig. 11 **a** Simulation crack growth behaviour of precracked specimen of initial crack length 1.2 mm subjected to load sequence with overload ratio 2.2 and subsequent cycles at R = −2, −1, 0 with same maximum load **b** Variation of traction with the separation at the crack tip for same cyclic loading conditions

parameter due to ductile fracture mechanisms as well as micro-structural fatigue damage.

The model implemented as interface elements is shown to represent the elastic–plastic behaviour of the process zone accurately under both tension and compression. Further, in the fatigue crack growth simulations in plane strain simulations of a notched CTS specimen, the difference between the retardation effects due to compressive overload and a tensile overload, as reported in literature, was well reproduced by the model. We show that accurate description of the elastic–plastic behaviour of the process zone is vital in prediction of retardation effects, in particular for the cases with negative stress ratios subsequent to a tensile over-load, as considerable plastic deformation occurs in compression resulting in significantly reduced retardation effects.

The effectiveness of the model in prediction of sequential effects under variable amplitude loading quantitatively in metal alloys is part of an ongoing study and is outside the scope of present work. Even though the implementation presented here uses plane strain idealisation which is computationally cost effective in reproducing effects of overload of different compression–tension combinations on crack growth curves, the formulation of the model is general and can be implemented for simulation of 3D effects such as evolution of crack front etc.

A Summary of the traction–separation behaviour.

Table 1 Summary of traction–separation law

(i) Elastic traction–separation relationship

$$\dot{T}_n = (1-D)\bar{E}(\dot{\hat{\delta}}_n - \dot{\hat{\delta}}_n^p) - \dot{D}\bar{E}(\hat{\delta}_n - \hat{\delta}_n^p)$$

(ii) Flow of inelastic separation

$$\dot{\hat{\delta}}_n^p = \frac{3}{2}\,\dot{\lambda}\,\frac{(2-\alpha-\beta)}{3\sqrt{\frac{(\alpha-1)^2+(\beta-1)^2+(\alpha-\beta)^2}{2}}}\,\mathrm{sign}(\mathrm{T_n})$$

(iii) Isotropic hardening law

$$\dot{\lambda} = |\dot{\epsilon}^p|$$

$$\bar{\sigma}_y = \bar{\sigma}_{y0}\left(1 + \frac{\lambda E}{\sigma_{y0}}\right)^n$$

(iv) Damage evolution law of the process zone

$$\dot{D} = \dot{D}_m + \dot{D}_f$$

$$\dot{D}_m = \frac{0.02\ \dot{\lambda}}{\epsilon_{y0}+\lambda_s}\left(\frac{\lambda-\lambda_s}{\epsilon_{y0}+\lambda_s}\right)^3 e^{-0.005\left(\frac{\lambda-\lambda_s}{\epsilon_{y0}+\lambda_s}\right)^4} H(\lambda-\lambda_s)$$

$$\dot{D}_f = \frac{\langle\dot{\delta}_n\rangle}{\delta_\Sigma}\ H\ (\delta_{acc} - \Delta_0) \qquad T_n \geq \sigma_f$$

$$\dot{D}_f = 0 \qquad T_n < \sigma_f$$

(v) Yield condition for the traction–separation law

$$\Phi := |T_n| - (1-D)\bar{\sigma}_y \qquad \lambda < \lambda_s$$

$$= |T_n| - (1-D)\bar{\sigma}_y^{max} \qquad \lambda \geq \lambda_s$$

(vi) Kuhn-Tucker complementary conditions

$$\Phi\dot{\lambda} = 0$$

B Consistent tangent operator

The incremental form of the stress-state dependent traction separation behaviour for the cohesive elements is shown in Eq. 3. The associated tangent modulus, K, is then defined as

$$K = \frac{\partial T_n}{\partial \hat{\delta}_n} \tag{16}$$

$$\frac{\partial T_n}{\partial \hat{\delta}_n} = (1-D)\bar{E}\left(1 - \frac{\partial \hat{\delta}_n^p}{\partial \hat{\delta}_n}\right) - \frac{\partial D}{\partial \hat{\delta}_n}\bar{E}\left(\hat{\delta}_n - \hat{\delta}_n^p\right) \tag{17}$$

and is implemented into FEM as per (Segurado and LLorca 2004). From Eqs. 8 and 11, $\frac{\partial \hat{\delta}_n^p}{\partial \hat{\delta}_n}$ and $\frac{\partial D}{\partial \hat{\delta}_n}$ are determined to be of the form

$$\begin{aligned}
\frac{\partial \hat{\delta}_n^p}{\partial \hat{\delta}_n} &= \frac{\partial \hat{\delta}_n^p}{\partial \lambda}\frac{\partial \lambda}{\partial \hat{\delta}_n} \\
&= \frac{3}{2}\frac{(2-\alpha-\beta)}{3\sqrt{\frac{(\alpha-1)^2+(\beta-1)^2+(\alpha-\beta)^2}{2}}}\text{sign}(T_n)\frac{\partial \lambda}{\partial \hat{\delta}_n} \\
\frac{\partial D}{\partial \hat{\delta}_n} &= \frac{\partial D}{\partial \lambda}\frac{\partial \lambda}{\partial \hat{\delta}_n} = \frac{0.02}{\epsilon_{y0}+\lambda_s} \\
&\left(\frac{\lambda-\lambda_s}{\epsilon_{y0}+\lambda_s}\right)^3 e^{-0.005\left(\frac{\lambda-\lambda_s}{\epsilon_{y0}+\lambda_s}\right)^4} H(\lambda-\lambda_s)\frac{\partial \lambda}{\partial \hat{\delta}_n}.
\end{aligned} \tag{18}$$

where $\frac{\partial \lambda}{\partial \hat{\delta}_n}$ is found by enforcing consistency condition to the triaxiality dependent one dimensional yield surface formulated, earlier in Eq. 15, so that during yielding traction remains on the yield surface. From consistency condition of the damage coupled yield surface, $\dot{\Phi} = 0$, $\frac{\partial \lambda}{\partial \hat{\delta}_n}$ is found and takes the form

$$\frac{\partial \lambda}{\partial \hat{\delta}_n} = \frac{(1-D)\bar{E}\ \text{sign}(\text{T}_\text{n})}{(1-D)\left(\bar{E}\ \frac{\partial \hat{\delta}_n^p}{\partial \lambda}\ \text{sign}(\text{T}_\text{n}) + \frac{\partial \text{N}_\text{y}}{\partial \lambda}\right) + \frac{\partial D}{\partial \lambda}\left(\bar{E}\ (\hat{\delta}_n - \hat{\delta}_n^p)\ \text{sign}(\text{T}_\text{n}) - \text{N}_\text{y}\right)} \tag{19}$$

References

Anvari M, Scheider I, Thaulow C (2006) Simulation of dynamic ductile crack growth using strain-rate and triaxiality-dependent cohesive elements. Eng Fract Mech 73:2210–28

Banerjee A, Manivasagam R (2009) Triaxiality dependent cohesive zone model. Eng Fract Mech 76:1761–70

Bao Y, Wierzbicki T (2004) On fracture locus in the equivalent strain and stress triaxiality space 46:81–98

Barsoum I, Faleskog J (2007) Rupture mechanisms in combined tension and shear-Experiments. Int J Solids Struct 44:1768–86

Beden SM, Abdullah S, Ariffin AK (2009) Review of fatigue crack propagation models for metallic components. vol. 28

Bouvard JL, Chaboche JL, Feyel F, Gallerneau F (2009) A cohesive zone model for fatigue and creep-fatigue crack growth in single crystal superalloys. Int J Fatigue 31:868–79

Danas K, Ponte Castañeda P (2012) Influence of the Lode parameter and the stress triaxiality on the failure of elasto-plastic porous materials. Int J Solids Struct 49:1325–42

De-Andrés A, Pérez JL, Ortiz M (1999) Elastoplastic finite element analysis of three-dimensional fatigue crack growth in aluminum shafts subjected to axial loading. Int J Solids Struct 36:2231–58

Elber W (1971) The Significance of Fatigue Crack Closure. ASTM Spec Tech Publ 230–42

Hancock JW, Brown DK (1983) On the role of strain and stress state in ductile failure. J Mech Phys Solids 31:1–24

Hancock JW, Mackenzie AC (1976) On the mechanisms of ductile failure in high-strength steels subjected to multi-axial stress-states. J Mech Phys Solids 24:147–60

Horstemeyer MF, Farkas D, Kim S, Tang T, Potirniche G (2010) Nanostructurally small cracks (NSC): a review on atomistic modeling of fatigue. Int J Fatigue 32:1473–502

Hutař P, Seitl S, Knésl Z (2006) Effect of constraint on fatigue crack propagation near threshold in medium carbon steel. Comput Mater Sci 37:51–7

Jha D, Banerjee A (2012) A cohesive model for fatigue failure in complex stress-states. Int J Fatigue 36:155–62

Jiang H, Gao X, Srivatsan TS (2009) Predicting the influence of overload and loading mode on fatigue crack growth : a numerical approach using irreversible cohesive elements. Finite Elem Anal Des 45:675–85

Lemaitre J (2012) A course on damage mechanics. Springer, New York

Li H, Li C, Yuan H (2017) Prediction of fatigue crack growth retardation using a cyclic cohesive zone model. Arch Appl Mech 87:1061–75

Li H, Yuan H (2013) Cohesive zone modelling of low cycle fatigue cracks in cracked and notched specimens. Fatigue Fract Eng Mater Struct 36:1246–57

Liu J, Xiang C, Yuan H (2009) Prediction of 3D small fatigue crack propagation in shot-peened specimens. Comput Mater Sci 46:566–71

Miarka P, Cruces AS, Seitl S, Malíková L, Lopez-Crespo P (2020) Influence of the constraint effect on the fatigue crack growth rate in S355 J2 steel using digital image correlation. Fatigue Fract Eng Mater Struct 1703–18

Needleman A (1992) Micromechanical modelling of interfacial decohesion. Ultramicroscopy 40:203–14

Newman JC (1984) A crack opening stress equation for fatigue crack growth. Int J Fract 24:131–5

Nijin IS, Banerjee A (2020) Mesoscopic mechanisms in fatigue crack initiation in an aluminium alloy. Fatigue Fract Eng Mater Struct 43(5):893–906

Nijin IS, Shravan Kumar R, Banerjee A (2019) Role of stress-state on initiation and growth of a fatigue crack. Int J Fatigue 118:298–306

Nguyen O, Repetto EA, Ortiz M, Radovitzky RA (2001) A cohesive model of fatigue crack growth 351–69

Pandey VB, Singh IV, Mishra BK, Ahmad S, Venugopal Rao A, Kumar V (2019) A new framework based on continuum damage mechanics and XFEM for high cycle fatigue crack growth simulations. Eng Fract Mech 206:172–200

Park K, Paulino GH (2011) Cohesive zone models: a critical review of traction-separation relationships across fracture surfaces. Appl Mech Rev 64:1

Peerlings RHJ, Brekelmans WAM, De Borst R, Geers MGD (2000) Gradient-enhanced damage modelling of high-cycle fatigue. Int J Numer Methods Eng 49:1547–69

Qian Z, Takezono S, Tao K (1996) A nonlocal damage mechanics approach to high temperature fatigue crack growth. Eng Fract Mech 53:535–43

Rashid FM, Banerjee A (2013) Implementation and validation of a triaxiality dependent cohesive model: experiments and simulations. Int J Fract 181:227–39

Rashid FM, Banerjee A (2017) Simulation of fracture in a low ductility aluminum alloy using a triaxiality dependent cohesive model. Eng Fract Mech 179:1–12

Roe KL, Siegmund T (2003) An irreversible cohesive zone model for interface fatigue crack growth simulation. Eng Fract Mech 70:209–32

Roth S, Kuna M (2017) Prediction of size-dependent fatigue failure modes by means of a cyclic cohesive zone model. Int J Fatigue 100:58–67

Segurado J, LLorca J (2004) A new three-dimensional interface finite element to simulate fracture in composites. Int J Solids Struct 41:2977–93

Shlyannikov VN, Zakharov AP (2014) Multiaxial crack growth rate under variable T-stress. Eng Fract Mech 123:86–99

Siegmund T (2004) A numerical study of transient fatigue crack growth by use of an irreversible cohesive zone model. Int J Fatigue 26:929–39

Siegmund T, Brocks W (1999) Prediction of the Work of Separation and Implications to Modeling. Int J Fract 99:97–116

Siegmund T, Brocks W (2000) Numerical study on the correlation between the work of separation and the dissipation rate in ductile fracture. Eng Fract Mech 67:139–54

Skorupa M (1999) Load interaction effects during fatigue crack growth under variable amplitude loading—a literature review. Part II: qualitative interpretation. Fatigue Fract Eng Mater Struct 21:905–26

Stephens RI, Chen DK, Horn BW (1976) Fatigue Crack Growth with Negative Stress Ratio Following Single Overloads in 2024-T3 and 7075-T6 Aluminum Alloys. Vol 595. American Society for Testing and Materials

Sunder R (2012) Unraveling the science of variable amplitude fatigue. J ASTM Int 9:20–64

Tong J (2002) T-stress and its implications for crack growth. Eng Fract Mech 69:1325–37

Ural A, Krishnan VR, Papoulia KD (2009) International Journal of Solids and Structures A cohesive zone model for fatigue crack growth allowing for crack retardation q. Int J Solids Struct 46:2453–62

Voorwald HJC, Torres MAS, Pinto Júnior CCE (1991) Modelling of fatigue crack growth following overloads. Int J Fatigue 13:423–7

Xu Y, Yuan H (2009) On damage accumulations in the cyclic cohesive zone model for XFEM analysis of mixed-mode fatigue crack growth. Comput Mater Sci 46:579–85

Yuan H, Li X (2018) Critical remarks to cohesive zone modeling for three-dimensional elastoplastic fatigue crack propagation. Eng Fract Mech 202:311–31